8-18-2020

High-frequency data reveal differential dissolved and suspended solids behavior from a mixed restored prairie and agricultural catchment

Andrew Miller
University of Nebraska at Omaha, andrewmiller@unomaha.edu

Ashlee L. Dere
University of Nebraska at Omaha, adere@unomaha.edu

Tracy Coleman
University of Nebraska at Omaha, tracycoleman@unomaha.edu

High-frequency data reveal differential dissolved and suspended solids behavior from a mixed restored prairie and agricultural catchment

Andrew Miller[1*], Ashlee Dere[2], Tracy Coleman[3]

[1]University of Nebraska at Omaha, Department of Chemistry, Omaha, NE, USA
[2]University of Nebraska at Omaha, Department of Geography/Geology, Omaha, NE, USA
[3]University of Nebraska at Omaha, Department of Biology, Omaha, NE, USA
*****corresponding author, andrew.walker.miller@gmail.com

Abstract

Quantifying temporal variability and fluxes within hydrologic catchments is critical to understanding the underlying chemical and physical processes leading to material transport. Measuring variability and fluxes requires sampling at time scales similar to the time scale of process occurrence. This demand has led to the development of automated sampling systems designed to sample at high frequencies, on the order of minutes. While widely deployed in a variety of systems, we installed two high-frequency sampling devices in a single drainage comprised of restored prairie and agricultural land uses in temperate Eastern Nebraska. The sampling systems determined flow rate, conductivity, and turbidity at 15-minute intervals for a twelve-month period. Conductivity was used as a proxy for total dissolved solids (TDS) concentrations and turbidity was used as a proxy for total suspended solids (TSS) concentrations. Using the high-frequency data, estimates of solids flux were calculated, error on the estimates was constrained, the effects of sample timing were considered, and conductivity and turbidity changes during precipitation events were examined. Overall, TDS fluxes were about three times higher than TSS fluxes from the catchment as a whole. However, the TSS fluxes were higher in the agricultural section of the catchment than from the restored prairie. Sheet and rill soil loss estimates from both the restored prairie and agricultural settings were low (<0.060 mm/yr). For TDS flux calculations, sampling at a monthly frequency gave a value that was only 11% lower than sampling every 15 minutes. For TSS flux calculations, sampling only during precipitation events (0.7% of the time) would capture 67% of the annual flux. Thus, minimizing error in sampling strategies depends on the constituent being analyzed.

1. Introduction

The use of high-frequency data logging devices to monitor environmental systems has become an increasingly widespread (Rode et al. 2016, Neal et al. 2012) research tool to study integrated systems such as the critical zone (Floury et al. 2017) or a hydrological catchment (Grathwohl et al. 2013, von Freyberg, Studer, and Kirchner 2017, Aubert et al. 2013). High-frequency measurements have been made over a variety of catchment scales, ranging from smaller, low stream order systems (~0.3-10 km^2) to nearly continental scale systems (>1000 km^2)(Miller et al. 2016, Pellerin et al. 2014, Snyder, Potter, and McDowell 2018, Jeong et al. 2012, Line, Hall, and Blackwell 2013, Floury et al. 2019, Miller et al.

2017, Schwientek, Osenbrück, and Fleischer 2013, Ziegler et al. 2014, Zimmer et al. 2019). Land uses surrounding high-frequency device deployments are predominantly agricultural, forested, and mountainous, with fewer examples of urban, wetland, and pastureland. Most deployed systems measure flow rates, and at least one chemical parameter, frequently dissolved oxygen (DO), conductivity, turbidity, or nitrate concentrations. Data analysis in high frequency sampling studies generally focuses on flux calculations, error analysis of flux estimates, the use of proxies to estimate behavior of a non-directly determinable compound, and the effects of short-term environmental events, most notably precipitation events.

In general, higher frequency sampling leads to less error on flux estimates (Harmel et al. 2009, Pellerin et al. 2014, Jones et al. 2012, Kerr et al. 2018). However, using the high-frequency data to generate guidelines for non-automated sampling strategies has generated recommendations of fixed sampling periods ranging from hours to weeks (e.g., Thompson et al. 2014, Li et al. 2019), or discharge dependent sampling frequencies (Schleppi, Waldner, and Fritschi 2006). Furthermore, the error associated with flux estimates may vary both with the identity of the water quality constituent (Kerr, Eimers, and Yao 2016) and with catchment size (Birgand et al. 2010). Sampling frequency also leads to different error distributions of measured parameters (Floury et al. 2017). In order to determine if a system is changing due to anthropogenic interventions, errors associated with pre- and post-intervention conditions must be consistently constrained to make comparisons feasible.

The use of chemical proxies is due largely to the limited number of devices commercially available to make automated measurements. The use of a proxy forges a link between what is measurable and what is actually necessary to know. For example, turbidity probes are commonly used to estimate total suspended solids (TSS) (Line, Hall, and Blackwell 2013, Rügner et al. 2013), and it has also been linked to particulate carbon and nitrogen (Snyder, Potter, and McDowell 2018), particulate phosphorus (Stubblefield et al. 2007, Jones et al. 2011) and total metal concentration (Nasrabadi et al.

2016). In order to make the connections between what an automated system can measure and what might be of environmental interest, a large number of physical samples typically need to be taken to find a relationship between the measured value and the variable of interest, which can partially defeat the purpose of an automated sampling system. Furthermore, the relationships between the measured value and the compound of interest are frequently non-linear and can potentially rely on more than one measured variable (e.g., see Table 1 in Horsburgh et al. 2010), which can complicate error analysis.

Once the connections are made between measurements and the compound of interest, automated systems can be used to study biogeochemical cycles occurring within short (~1-24 hr) timeframes (Nimick, Gammons, and Parker 2011, Burns et al. 2019, Gribovszki, Szilágyi, and Kalicz 2010, Dupas et al. 2016, Lloyd et al. 2016, Liu et al. 2020). Working at these timeframes allows for mechanistic attribution of short scale variability. For example, diel variability in turbidity has been attributed to the daily activities of a nocturnal fish species (Loperfido et al. 2010). Also, examining high-frequency data during and immediately after precipitation events can lead to a better understanding of both water flow paths over or through soils as well as solute leaching behaviors. For example, the source and leaching behavior of natural organic matter has been identified by examining data at one-hour intervals after rain events. By spectroscopically separating more humic-like carbon from more tryptophan-like carbon, and examining concentration-discharge plots (i.e., hysteresis loops), sewer overflows during large or long precipitation events in urban areas are identifiable, while humic-like carbon leaching from surrounding soil is exhausted under the same conditions (Khamis, Bradley, and Hannah 2020).

In the manner of previous work, we deployed two high-frequency logging devices to measure flow rate, conductivity, and turbidity to determine solids (TSS and TDS) fluxes from a small (2 km^2) catchment comprised of both agricultural and restored prairie land uses in Eastern Nebraska. The site is in the process of conversion from agriculture to a restored prairie (Dickson, Hayes, and Bragg 2019). Several national and international programs exist to foster this land use conversion (e.g., Flávio et al.

2017, USDA 2016) with typical restoration goals including improving soil quality, minimizing soil losses due to erosion with subsequent sedimentation of waterways, and minimizing nutrient loading to water bodies. The goal was to develop baseline data prior to full site restoration to prairie and to compare the water quality impact of the previously restored prairie with current active agriculture land use. Data was collected at 15-minute intervals for one calendar year and was analyzed to determine 1) diel variability of water quantity and quality, 2) solids flux estimates from sub-sampling the high-frequency dataset, 3) the effects of precipitation events on solids exports, and 4) estimate soil erosion from the two land uses. Furthermore, we present a novel method to connect the proxy of turbidity to TSS. Our method requires minimal physical sample removal, making it more in line with the goals of automated sample collection.

2. Methods

2.1 Site description

Glacier Creek Preserve (GCP) is a 2.12 km^2 preserve containing the entire first order watershed of Glacier Creek. GCP is located in Eastern Nebraska, 20 km northwest of Omaha, NE (Figure 1). The preserve has two dominant land uses: row crop agriculture and restored tallgrass prairie. The agricultural land is managed using minimal till corn (*Zea mays L.*) and soybean (*Glycine max (L.)*) crop rotation. The restored prairie was converted from row crop agriculture to mixed tallgrass prairie in 1970; a controlled burn every three years is employed to maintain grass vegetation (Bragg, Maier, and Johnson 2016). Glacier Creek is a perennial stream fed by groundwater, with a streambed of silty loess overlying compact glacial till. Mean annual temperature at the site is 10 °C and mean annual precipitation is 78 cm.

2.2 Automated data collection

A YSI (Yellow Springs, OH, USA) EXO2 multiparameter sonde was placed in an oversized PVC pipe with large holes drilled throughout to allow for free water movement. The PVC pipe was secured to a weight to keep the sonde in place on the streambed and to elevate the sonde about 5 cm above the

stream bed. The sonde has an optical turbidity probe and a combined conductivity/temperature probe installed. Both probes were calibrated approximately monthly using purchased turbidity (124 FNU, styrene divinylbenzene copolymer beads) and conductivity (10,000 µS/cm) standards. The sonde was programmed to record data at 15-minute intervals immediately after a small brush rotated to remove sediments and biofilm that may have accumulated on the measurement end of the probe. The data was logged on a YSI Storm 3 Data Logger and downloaded monthly when the sonde was calibrated.

Immediately downstream from the sonde, a SonTek Xylem IQ (San Diego, CA, USA) *in-situ* sonar-based flow velocity meter was installed in the streambed. Like the sonde, the flow meter was also programmed to log water flow on 15-minute intervals, and the data was sent to the same Storm 3 data logger for monthly download. The flow meter was periodically inspected, and any sediment that had settled on the top of the meter was removed. The inspection and cleaning were more important after any rain or high flow events.

Weather and precipitation events were recorded using meteorological stations on the surrounding ridgetops in both the restored prairie and agricultural land uses. The Campbell Scientific (Logan, UT, USA) meteorological stations record data on a CR1000 datalogger with the following sensors: anemometer (R.M. Young's 03002 Wind Sentry Set), all season pyranometer (SP230), precipitation sensor (Texan Electronics Tipping Bucket Rain Gages), temperature and relative humidity sensor (HC2S3), and barometer (CS106). Atmospheric conditions were recorded hourly.

2.3 Manual sample collection

Similar to prior sample collections at the site (Dere et al. 2019), monthly stream samples were collected slightly downstream from the sonde (position GC1), from four sites upstream from the confluence of the two forks (GC3/GC4- agriculture, GC5/GC6- prairie), and from one site just below the confluence of the two forks (GC2) to determine individual major ion concentrations. Each sample was collected in a conditioned sampling beaker and filtered using a 0.45 µm PVDF syringe filter. Each sample

was split with one of the two being acidified (pH<2) with concentrated HCl for cation analysis. The unacidified sample was used for an alkalinity titration and for anion analysis. All samples were stored at 4°C prior to analysis. At the time of sampling, a Xylem (Rye Brook, NY, USA) ProDSS handheld meter was used to record basic water quality parameters, including pH/oxidation reduction potential, temperature/conductivity, turbidity and optical dissolved oxygen (DO). The probes were placed directly in the stream, and the data was recorded after several minutes allowing for both probe equilibration and the displacement of any water/sediment affected by the placement of the probes. In between the monthly sampling events, the same locations were monitored with only the handheld meter.

2.3.1 Lab analysis

For the stream water samples, major ions (Na^+, K^+, Mg^{+2}, Ca^{+2}, Cl^-, NO_3^-, and SO_4^{-2}) were determined using a Dionex Aquion ion chromatograph Alkalinity was determined within 24 hours of sampling, and was completed with a Hannah Instruments (Woodsocket, RI, USA) autotitrator with standardized HCl. The field pH and alkalinity were used to determine the concentrations of the carbonate species (HCO_3^- and CO_3^{-2}).

2.3.2 Calibrating conductivity and TDS

Stream samples were collected for lab analysis from June of 2017 to May of 2019. The alkalinity, field determined pH, DO, and temperature, and the measured concentrations for the major ions were used as input into PHREEQC (Parkhurst and Appelo 2013) to speciate the ions in the water and to determine the concentrations of the carbonate species. From the PHREEQC calculations, the average charge balance error was 4.8% implying that the analytical determinations were likely complete and accurate. From the individual ion concentrations, the TDS could be calculated for an individual sample by summing all of the individual concentrations, and assuming that one half of the total carbonate would be lost as CO_2 upon drying according to equation 1 (Hem 1982):

$$2HCO_3^- \leftrightarrow CO_3^{-2} + H_2O + CO_2 \quad (1)$$

A few confirmatory TDS analyses were also completed to compare to the calculated value. Filtered stream water (80-100 mL) was placed in a tared evaporation dish. The dish was placed in an oven at 180°C until no water was visible (~2-4 hours). The dish was cooled in a desiccator, and the mass of the dish and evaporated residue was determined.

Using the calculated TDS value and the conductivity as measured by the sonde at the nearest 15-minute time stamp to when the sample was taken, a ratio of TDS/conductivity was determined. From the 22 samples (one was not used due to missing conductivity data), an average and standard deviation for the ratio was determined.

2.3.3 Calibrating turbidity and TSS

To calibrate the turbidity values, native solids were collected from the stream via centrifugation. Working in batches, approximately 16 L of stream water were centrifuged at a g-force and time combination to remove particles >0.45 μm (90 minutes, 12,300 g). The particle-free water was decanted, collected and stored at 4°C. The collected solids were all transferred to a single tared centrifuge bottle. After centrifuging, the final water was removed and the solid was allowed to dry at room temperature for about 24 hours. The centrifuge bottle containing the solid was then placed in a desiccator with fresh desiccant for at least 48 hours. The desiccant was replaced and the solid was massed every 24-48 hours until the solid had reached a constant mass. To create a standard with the native solid material, the reserved particle-free water was added to the centrifuge bottle and the solid was resuspended and quantitatively transferred to a volumetric flask. The solid was sonicated for 15 minutes to disaggregate any particles, and the flask was brought to the calibrated volume. The native TSS standard was stored at 4°C for 24 hours to allow for complete solids hydration. This entire process was repeated twice with samples collected at two different times (25-Jun-2019, 16-Jul-2019) to examine the optical variability of the native particles.

Immediately after the sonde had been calibrated, turbidity measurements were made using the native TSS standard. The native standard was poured into the sonde calibration cup. After a brief period of mixing, agitation of the sonde cup ceased to allow for probe stabilization. The turbidity value was read immediately, before significant settling could occur. The native standard was then placed on a stir plate, and aliquots from the mixed solution were quantitatively diluted with the reserved particle-free water. The mixing/measurement/dilution process was repeated to create a calibration curve covering the range of values measured in the stream. Two separate calibration curves were created, one for each solids collection event.

Confirmatory TSS analyses were also completed to check the calibration curve. Periodic samples were taken from the stream to determine TSS. Depending on the solids concentration, 600-1000 mL of stream water were filtered through a tared 0.45 µm nitrocellulose filter. The filter was dried in an oven at 105°C for 1 hour, then cooled in a desiccator. The sample was brought to a constant mass in the desiccator as confirmed by subsequent massing in 24-hour intervals.

2.4 Automated data analysis

2.4.1. Initial Quality Assurance/Quality Control

The general data analysis goals from the automated data were to 1) estimate annual TSS and TDS fluxes from GCP at the highest time resolution possible, 2) examine the effect of different sampling time periods on the annual flux estimates, and 3) examine the effect of precipitation events on stream flow and solids behaviors. Data was collected from the automated systems from September 2017 to June of 2019. However, in that time period, the sonde was removed for a 3-week period in December 2018/January 2019 for factory re-calibration. Also, initial examination of the flow data showed significant periods of zero or negative flow values at various times throughout the measurement period. In an attempt to avoid as many prolonged data voids as possible, the period of December 1, 2017 to November 30, 2018 was used for much of the following analysis (n = 34,944 time points).

Flow, turbidity, and conductivity were graphically examined as a function of time to find clear data issues. For example, zero and negative values for volumetric flow, small negative numbers in measured turbidity, and conductivity values <100 µS/cm. The stream is a perennial stream, so zero and negative flow values are likely due only to measurement errors. Similarly, occasional negative turbidity values do not make sense, and the negative turbidity values did not appear to be related to faulty calibration. Finally, conductivity of local precipitation is approximately 50 µS/cm, so values <100 would be approaching pure precipitation, which is unlikely in a gaining stream. The aberrant conductivity and flow values were deleted from data set. The small negative turbidity values were replaced with a reading of zero.

The truncated dataset was then corrected for calibration events. During the calibration process, the sonde gives the pre and post calibration value for the probe being calibrated. The pre/post values for both the conductivity and turbidity probe for all of the relevant calibration events are given in the Supporting Information. In general, calibration drift was low (averages: 3.7% for conductivity and 2.1% for turbidity). The data was corrected for calibration drift by assuming a time weighted relative change in the measured values according to equation 2:

$$V_c = V + \left(\frac{V_f - V_s}{V_s}\right)\left(\frac{t_t - t}{t_t}\right) \qquad \text{eq. (2)}$$

where V_c is the corrected data value, V is the original measured data value, V_f is the reading of the sensor before calibration, V_s is the reading of the sensor immediately after calibration, t_t is the total time of deployment, and t is the time between the end of deployment and measured data value. While others have determined the calibration drift by measuring a standard prior to cleaning the probes (Horsburgh et al. 2010), the sonde was so dirty that acquiring a reading without significantly contaminating the standard was not feasible. The calibration order was to 1) clean the probes, 2) determine V_f of the standard, and 3) adjust the calibration to the new value, V_s. Due to the calibration

order, the mathematical correction for calibration drift does not correct for sediment or biofilm buildup on the probe that was not removed by the rotating brush.

2.4.2 Filling data gaps

For conductivity and turbidity nearly all of the remaining data gaps occurred during calibration events when the sonde was removed from the stream. Calibration events lasted about 2-4 hours. For calibration related gaps, conductivity and turbidity were estimated by linearly interpolating between recorded time points. For turbidity, small negative values were replaced with zero, and no interpolations were made based on the zero values. For short gaps (<1 hour) in the flow data, the flow was linearly interpolated between available data. For gaps that were 1-24 hours in length, the average of the flow immediately before and after the gap was used. Within the period of interest, there were 5 time periods when flow data were missing for >24 hour periods (31-Dec-17 to 7-Jan-18, 11-Jan-18 to 18-Jan-18, 10-Mar-18 to 12-Mar-18, 13-Mar-18 to 16-Mar-18, and 27-Sep-18 to 5-Oct-18). With the exception of the period beginning on 27-Sep-18, there was no measurable precipitation at the site during these time periods. During the period starting on 27-Sep-18, there was a rain event recorded lasting from 30-Sep-18 at 17:00 to 1-Oct-18 at 12:00. The total rainfall for this event was 13.5 mm, however the average precipitation rate was 0.75 mm/hr which is lower than the value that typically leads to clear increases in flow rate (see discussion). Thus, for all of the >24-hour data gaps, the flow was assumed to be equal to the monthly average.

2.4.3 Flux calculations

The first step in calculating flux was the conversion of the measured conductivity or turbidity value into TDS or TSS units, respectively. For conductivity, the ratio determined above was multiplied by each conductivity value to get the dissolved solids concentration in mg dissolved solid/L. For TSS, the turbidity value was converted using the calibration curves as described above. The TSS value was also in mg suspended solid/L. The solids concentration, flow and time interval were used to calculate the total

249 solid exported during the time interval, and all of the time intervals were summed to get an annualized
250 flux using equation 3:

251 $$W = \sum_{i=0}^{n} Q_i \, C_i x \quad \text{(Eq. 3)}$$

252 where W is the total annual load (kg), Q_i is the incremental flow rate (m^3/sec), C_i is the incremental
253 solids concentration (mg/L), x is a factor to convert to kg solid per appropriate time period, and n is the
254 total number of time steps in the one-year monitoring period.

255 In order to determine the error on the flux calculation, three separate errors were combined
256 using standard error propagation. Those three errors were the measurement error, the error in the
257 conversion of the measured value to solids concentration, and the error associated with the flow
258 measurement. For the error in the conductivity probe measurements, the manufacturer's stated
259 precision is 0.5% of the measured value, and for the turbidity probe the precision is stated as 2% from 0-
260 999 FNU. Due to being deployed in field conditions, both of these error estimates were increased to 5%
261 of the measured value for error analysis. For the TDS conversion, the standard deviation for the 22
262 calculated TDS/conductivity ratios was also 5% of the ratio value. For TSS concentrations, due to the
263 outcomes from the calibration curves discussed in more detail below, a fixed 25% error was assumed for
264 the conversion of turbidity to TSS. For flow measurements, the manufacturer claims precision levels of
265 1%. However, much of the flow in Glacier Creek is small (annualized average flow rate of ~0.008 m^3/s),
266 and the flow meter only outputs the flow to the nearest 0.001 m^3/s. Therefore, the flow rate error was
267 assumed to be an absolute error of $\pm$0.001 m^3/s. The errors were combined using equation 4:

268 $$s_{flux} = \sqrt{e_m^2 + e_c^2 + e_f^2} \quad \text{(eq. 4)}$$

269 where s_{flux} is the relative error in the calculated flux, e_m is the relative error in the measurement, e_c is the
270 relative error in the conversion of the measurement to solids concentration, and e_f is the relative error in
271 the flow rate. The error was calculated for each individual time step. When the annualized flux was

calculated by adding the individual time steps (equation 3), the error for the time steps was propagated using equation 5:

$$s_{ann.flux} = \sqrt{\sum_i^n s_{flux,i}^2} \quad \text{(eq.5)}$$

where $s_{ann.flux}$ is the absolute error in the annualized flux, $s_{flux,i}$ is the absolute error in the flux for the i^{th} time step, and n is the total number of time steps.

To examine the effect of sampling rate on load estimates, the data was sub-sampled at increasing time intervals ranging from hourly to monthly. For hourly flux calculations, only one of every four 15-minute timepoints was used to calculate flux. Since the original dataset had measurements every 15 minutes, this led to four realizations: one each for sampling on the hour, and 15, 30, or 45 minutes past the hour. For daily flux calculations, the flux was calculated for the day at two-hour intervals (i.e., every day at midnight, every day at 2:00, etc.) leading to 12 realizations. For weekly flux calculations, flux was calculated using data from every 7^{th} day at three different times of day, 9:00, 12:00, and 15:00. These times were chosen to represent different sampling times within a standard working day. This process led to 21 realizations. And finally, monthly flux values were calculated for every other day of the month (i.e., 1^{st}, 3^{rd}, 5^{th}, etc.) at three different times of day (9:00, 12:00, 15:00). This led to 44 realizations. For these different averaging methods, the standard deviation and 90% confidence interval were calculated based on the variability of the realizations.

2.4.4 Concentration changes with flow (hysteresis loops)

From the weather station data, there were 46 precipitation events within the studied time period that lasted for three or more hours, or that were >5mm in total precipitation. Details on the timing of the precipitation events, their duration and the amount of precipitation are available in the Supporting Information. For 16 of the 46 events, hysteresis loops (turbidity/conductivity vs. flow) were plotted. The 16 events cover the range of precipitation totals and precipitation rates from the 46 events.

Also included in the hysteresis plots are two events where flow increased due to snowmelt (26-Feb-18 and 14/15-Feb-18). Several of the precipitation events occurred in quick succession, being separated by less than 24 hours. These multiple events are shown on a single plot to show the effects of closely spaced sequential events.

3. Results

3.1 Manual sampling

The relative amount of the total stream flow was split between the north (agriculture) and south (restored prairie) forks using mass balance calculations and the concentrations of conservative ions (Na^+ and Cl^-) at positions GC2, GC3 and GC5. From those calculations, an annualized average of 66% ($\pm$ 12%) of the total flow came from the north fork and 34% ($\pm$ 12%) came from the south fork. This flow distribution is consistent with what was observed in previous years (Dere et al. 2019).

For the general water quality measurements, conductivity and turbidity were grouped at sampling locations GC3/GC4 and GC5/GC6 to represent the agriculture and restored prairie drainages, respectively. Any questionable turbidity values (values <0, and values from 30-Mar-18 which appeared to be a bad calibration) were excluded from the analysis. The averages and standard deviations are shown in Table 1. The conductivity values are significantly different ($p<0.05$) while the turbidity values are not ($p = 0.61$).

3.2 Conductivity to TDS conversion

From the measured ion concentrations at sampling GC1, the TDS/conductivity ratio was determined to be 0.519 ± 0.0023 ($\pm 1\ s.d.$, n = 22). The experimentally determined value is 0.573 ± 0.0016 ($\pm 1\ s.d.$, n = 4). The average values from the two methods are significantly different ($p = 0.001$).

3.3 Turbidity to TSS conversion

The two TSS calibration curves for the two separate solid samples are shown in Figure 2. The curves from the two solids collections have different slopes implying some optical variability in the

319 solids. However, the grab samples tend to cluster along the curve associated with the second solids
320 collection. Those samples were collected periodically over a two-month period. During that time, some
321 were associated with rainier weather and some were associated with drier weather. The closeness of
322 the individual values to the calibration curves gives some degree of confidence in using the curves for
323 the turbidity to TSS conversions.

324 For the purposes of the turbidity conversion, two different equations were used depending on
325 whether the measurement was above or below 20 NTU (Table 2). For values below 20 NTU (~92% of all
326 measurements), the calibration curves needed to be forced through zero to avoid small negative
327 concentrations for very small (<~2 NTU) turbidity values. The equation used to perform the conversion
328 was obtained from treating all of the data points at <20 NTU as a single data set whether they were grab
329 samples or the calibration standards. A line of best fit, forced through zero, was fit to the data, which
330 functionally 'averaged' the slopes of the two calibration curves. In terms of handling the error associated
331 with the slope of the line, two options were considered. The first was to use the standard error in the
332 slope based on the statistics associated with fitting lines to data; this process led to an error estimate of
333 14% of the slope value. The second was to use the range of the slopes from the two calibration curves to
334 bound the value for the slope of the line; this method led to an error estimate of 25% of the slope value.
335 In the interest of conservative error estimation, the 25% value was used in the error propagation
336 discussed in section 2.4.3. For measured values larger than 20 NTU, the line of best fit for the calibration
337 curve with the larger solids range was used. Since the measured values were larger, there was no need
338 to force the curve through zero. As before, the range of the slopes for the two calibration curves were
339 used to estimate the error. The range of the slopes between the calibration curves varied by 15%, but
340 for consistency and to get a conservative estimate of error, this was increased to 25% in the error
341 propagation.

342 *3.4 Time series*

Figure 3 shows the uncorrected and corrected measured conductivity values for the time period studied. Figure 4 shows only the corrected turbidity values; for the scale shown, there is no visible difference between the corrected and uncorrected turbidity values. Figure 5 shows the measured flow rate for the time studied. Large spikes in flow associated with rain events generally coincide with downward spikes in conductivity and positive spikes in turbidity. However, there were also many turbidity spikes unrelated to changes in flow. These unassigned turbidity spikes did not necessarily appear to be random individual mismeasurements by the probe. The positive spikes are typically substantiated at multiple timepoints. Besides the expected connection between rainfall and flow, the high frequency measurements also showed a sinusoidal diel behavior with flow peaking slightly after sunrise (~7:00 - 9:00) and minimizing after sunset (~20:00 - 23:00). While small in magnitude, this pattern was frequently observed soon after rain events during the growing season (~April-October).

3.5 Flux calculations

The calculated flux estimates associated with different sampling time intervals are shown in Table 3. The error associated with the 15-minute sampling intervals is the formally propagated error as described in section 2.4.3. For all other sampling intervals, the standard deviation and 90% confidence interval for the different realizations are used to estimate the error in the flux values. Dissolved solids fluxes appear to be less affected by sampling interval than do the suspended solids fluxes. The monthly time interval flux estimate for dissolved solids is about 10% less than the 15-minute sampling interval, while the suspended solids flux decreases by an order of magnitude. When looking at the error ranges, the confidence intervals, which should correct for the changing values of n, generally increase as the sampling time interval increases. However, for both dissolved and suspended solids, the confidence interval drops moving from weekly to monthly sampling intervals.

3.6 Behavior during precipitation events

In general, hysteresis loops for conductivity and turbidity for most of the rain events led to clockwise hysteresis patterns (Fig. 6). For conductivity, the clockwise behavior meant that the conductivity was decreasing as flow was increasing, and then increasing as flow returned to base flow. For turbidity, the clockwise behavior was due to increasing turbidity with increasing flow, then decreasing turbidity as flow returned to base flow. However, for some rainfall events turbidity exhibited a counterclockwise hysteresis while conductivity hysteresis was clockwise (Fig. 7). The changes in flow due to snowmelt exhibit the same clockwise patterns as those due to rain events, although both conductivity and turbidity switch to counterclockwise hysteresis during one of the snowmelt events (Fig. 8). For rain events that are closely spaced in time, the loops maintain the clockwise directionality, but the width and height of the loops contracts in later rain events. For about half of the 16 rain events, there was no evident change to flow or measured chemical parameters; all of these rain events were associated with rainfall intensity <1.5 mm per hour (Fig. 9).

4.0 Discussion

4.1 Measurement conversion to solids concentration

Converting the conductivity to TDS seemed reliable with the exception that the experimentally determined TDS/conductivity ratios were different from the calculated ratios using individual ionic concentrations. While not reported here, iron, manganese and aluminum are all regularly determined for stream samples using ICP-MS (Dere et al. 2019), and while aluminum is generally non-detectable, iron and manganese have concentrations that are always <2 mg/L and are typically ~0.5 mg/L (or ~0.01 mM). These low concentrations would not make significant contributions to the dissolved solids. The major components that might be present in the stream water that were not measured regularly or at all are forms of organic carbon and silicon. Organic carbon concentrations are measured periodically and, in this stream, tend to be low (<5 mg/L, unpublished data). Silicon has never been determined, but for the circumneutral pH range in Glacier Creek (~6.5-7.5), silicate solubility is limited to about 1 mM. Using the

390 5 mg/L organic carbon concentration and 0.3 mM Si (assuming it is present as H_4SiO_4), the
391 experimentally determined ratios are identical to the calculated ratios. It seems likely that the difference
392 between the two numbers is largely due to dissolved silicon. Since the conversion between conductivity
393 and TDS is linear, the 10% increase from the calculated ratio to the experimentally determined ratio
394 would also increase the flux estimate by 10%.
395 The conversion of turbidity to TSS by making site specific TSS standards is a departure from the
396 more common method of taking TSS measurements periodically over long periods of time. The clear
397 advantage of the method presented here is that a calibration curve can be created in a short time
398 period, and the site of interest does not need to be manually sampled as frequently. The significant
399 disadvantages are that the temporal optical variability of the solids cannot be captured, and that the
400 processing of the solids samples may have altered the associated particles. The second of these
401 concerns was directly tested with the grab samples removed from the stream. Since they are nearly in
402 line with at least one of the calibration curves, it seems likely that alterations to the particles are
403 minimal. However, without testing the stream over long periods of time, the first of these disadvantages
404 is not easy to constrain. In the literature there is a large variety of model fits to relate turbidity to TSS,
405 including log transforms and exponential functions (Horsburgh et al. 2010). For references that used
406 only linear fits, the range of slope values is ~0.8-5 $mg*L^{-1}*NTU^{-1}$ for land uses ranging from agricultural to
407 forests with various soil types and local topography (Nasrabadi et al. 2016, Schwarz, Gocht, and
408 Grathwohl 2011, Stubblefield et al. 2007, Lin et al. 2011, Line, Hall, and Blackwell 2013, Rügner et al.
409 2013, Jones et al. 2011). The values used here for the slopes of the calibration curve (0.28 $mg*L^{-1}*NTU^{-1}$
410 and 0.60 $mg*L^{-1}*NTU^{-1}$) are below the range found by others. It is unclear if this difference is due to
411 differences between the systems or differences between the methods used. In order to estimate the
412 error associated with a less certain slope, the error in converting the turbidity to TSS can be doubled

413 from 25% to 50%. This change increases the error in the flux estimate from 4.0% to 7.9%, essentially
414 linearly. This higher level of error is closer to the error associated with missing data (see below).
415 *4.2 Error associated with automated sampling*
416 For the three measured parameters, conductivity, turbidity and flow, flow measurements were
417 the most likely to be missing or give unreliable numbers while conductivity was the least likely (Table 4).
418 Conductivity was only missing during calibration events, and at a few sampling points (~5) when the
419 conductivity level was less than 100 µS/cm. Flow and turbidity data gaps are exacerbated by the size of
420 Glacier Creek. Glacier Creek is a smaller stream than most other streams where automated data
421 collection has been employed; the base flow rate in the stream is nearing the smallest value that can be
422 detected by the SonTek device. Anytime flow drops below 0.001 m^3/s, the measurement would show no
423 flow and the data point would be rejected. Furthermore, the small size of the stream means there is not
424 a good deployment orientation that will minimize the effects of sediment deposition after rain events
425 when data seemed more error prone. Visually the flow meter would frequently have a layer of sediment
426 that would need to be manually removed after rain events. Turbidity measurements immediately after
427 rain events were frequently an order of magnitude higher than before the rain event, and that condition
428 frequently persisted for 24 hours or more. There are also several places in the record where the
429 turbidity suddenly (within 15 minutes) drops back to the levels measured before the rain event. This is
430 likely due to manual cleaning of the area surrounding the probe. The automated brush alone did not
431 appear to be sufficient at clearing out the potentially large sediment loads. While missing or
432 questionable flow data were simply rejected from analysis, the values associated with the turbidity were
433 still used despite the appearance of being affected by sediment. This likely leads to a positive bias in the
434 TSS flux values.
435 Besides the formal errors addressed in the flux calculations, the missing data also creates an
436 'error' associated with data extrapolation. During short time periods, the extrapolated data likely

creates small variation in the resultant flux, but the longer time periods might start to introduce deviations from reality. Flow data was the most likely to be missing, however the majority of that missing data was for short time periods, with >1 hr durations accounting for 6.7% of the total number of measurements (Table 4). For the measured chemical parameters, missing flow and/or missing the conductivity or turbidity value would cause the flux to be an extrapolated value. But since the chemical measurements were generally more reliable, missing only the turbidity measurement accounts for 0.1% of the total TSS flux and missing only the conductivity measurement accounts for 0.5% of the total TDS flux (Table 4). Thus, the error in flux quantities calculated from missing flow data, which had to be filled in, is larger than the formal error associated with the flux calculations (Table 3, 0.1% TDS, and 4.0% TSS). Therefore, the formal error analysis may underestimate the overall uncertainty associated with the data set.

A final 'error' in the dataset is the extrapolation of the turbidity calibration to the higher levels that are observed in the stream. The probe is calibrated with a two-point calibration at 0 and 124 NTU. Stream values are typically well below the upper calibration standard, but after rain events the turbidities can be an order of magnitude higher (Figure 4). The manufacturer claims the probe is linear up to 999 NTU, and clearly in the solids calibration curve it is linear up to about 500 NTU. However, for values above 500 NTU, the data may become more non-linear. The number of turbidity measurements at levels beyond the calibration curve only account for 0.7% of the monitoring period. But, those same measurements account for 67.0% of the total annual flux. Thus, better calibration at higher levels is required for better constraint of the error during periods of high solids export. Furthermore, if automated sampling was not in use, the observation that 67.0% of the total flux occurs in 0.7% of the time lends support to the sampling strategy of sampling during or immediately after rain events to estimate TSS loads. In fact, the flux associated with missing data is ~20-40% (Table 4), which is similar to

460 the amount of flux that would not be directly determined if sampling only occurred during/after rain
461 events.
462 Other possible sampling strategies were explored by sub-sampling the data at time intervals
463 longer than 15 minutes. If the value observed using all of the data is considered to be 'true', then
464 sampling conductivity at hourly, daily, or weekly time scales only changed the flux estimate by about 1%.
465 Even sampling monthly gave an average flux that was only 11% lower than the 'true' value. A similar
466 range of propagated error (3 – 20%) was reported by Fluory et al. (2017, 2019) when comparing annual
467 output fluxes for a range of solute species sampled every 40 minutes or monthly.
468 For turbidity however, the behavior was dramatically different. Daily and weekly sampling gave
469 estimates that were 78% and 96% higher, respectively. Then at a monthly sampling rate, the value drops
470 80% below the 'true' value. In terms of error of the different sampling timescales, the error estimates
471 generally got larger as the time scale was lengthened, however at the monthly timescale the error
472 decreased. This is true both of the standard deviation associated with averaging the different
473 realizations, and also with the 90% confidence interval which considers the differing number of
474 realizations used. When other have done a similar analysis, the overall fluxes decreased consistently and
475 the error bars consistently increased as the sampling time period got longer (Jones et al. 2012). Their
476 calculation method involved more realizations than were used here, so it is unclear if our number of
477 realizations is too small to represent the population, or if there is a fundamental difference between the
478 two systems.
479 Based on this annual data for the Glacier Creek watershed, there does not appear to be a
480 consistent sampling strategy that would both minimize the amount of fieldwork if sampling were not
481 automated and still give a realistic estimate for the flux. For conductivity, sampling monthly appears to
482 be a good tradeoff in accuracy and number of samples required. For turbidity, sampling during or
483 immediately after rain events might be the better option. The difference in behavior between the two

parameters may be related to the nature of the stream and the source of the TDS/TSS material. The dissolved solids originate as weathering products in the soil matrix, which then migrate to the stream in groundwater. Much of the suspended solids are directly generated and transported from overland flow. The flashier nature of the surface water flow may lead to more variability in the flux compared to the dampened migration of the dissolved ions that may be temporarily stored in the groundwater.

4.3 Behavior during precipitation events

Hysteresis loops can highlight how solutes and sediments respond to increases in stream flow due to rainfall events. In general, we observe clockwise hysteresis patterns, and this appears to be related to precipitation rate: for rates >1.5 mm/hour hysteresis was generally observed (Fig. 6, 7); when rates were <1.5 mm/hour no evident changes to flow or measured chemical parameters were observed (Fig. 9). Clockwise hysteresis patterns for conductivity and turbidity are also generally observed following snowmelt events, although one snowmelt event shows complex hysteretic behavior where conductivity and turbidity switch to counterclockwise behavior (Fig. 8).

During storm events that exceed the precipitation intensity threshold, conductivity hysteresis is generally clockwise, with conductivity decreasing then increasing as flow increases then decreases, suggesting that the dissolved solutes may be initially flushed during a storm event as dilute precipitation enters the stream, then conductivity rises again when solute-rich groundwater once again becomes the main source of flow to the stream (Wymore et al. 2019). Turbidity also generally exhibits clockwise behavior, with turbidity increasing with increasing flow, then decreasing as flow returns to base flow, suggesting that sediment is flushed as flow increases. However, in contrast to the clockwise hysteresis loops for conductivity, turbidity sometimes exhibits counterclockwise hysteresis loops, where turbidity continues to increase despite a decrease in flow to mobilize sediment (Fig. 7). This behavior could be explained by sediment mobilization from the hillslopes and particle movement in the subsurface in addition to sediment sources in the stream channel mobilized by energy of the rising stream flow

(Wymore et al. 2019). Additional data will help untangle the mechanisms driving hysteresis loop directionality and response to storm events.

4.4 Geochemical relevance

The main goal of tracking solids concentrations in the Glacier Creek was to determine the major modes of solids export (dissolved vs. particulate) and to estimate solids loss associated with land use type (restored prairie vs. agriculture). Based on the data, it is clear that solids export is dominated by dissolved weathering products. The TDS export was about three times higher than the suspended solids export. Furthermore, the difference between the two is likely a low-end estimate due to the positive bias on the TSS estimate due to the sediment deposited after rain events, and the TDS having a negative bias due to not including the silicates. In terms of comparing the exports of the restored prairie vs. agriculture, the two forks of the creek can be evaluated. Using the data from the spatial sampling within the two forks, the north fork (agriculture) had significantly lower conductivity than the south fork (restored prairie, $p<0.01$, $n = 44$ from both forks). This was expected, as the details of individual ionic fluxes from the two land uses was examined previously and concluded that dilute overland and shallow groundwater flow from the agricultural hillslope is likely lowering conductivity in the fork draining agriculture, whereas water on prairie covered hillslopes is infiltrating and interacting with deeper minerals before entering the south fork of the stream, increasing stream conductivity (Dere et al. 2019). However, the measured turbidities in the two forks were not significantly different ($p = 0.61$, $n = 29$ north fork, and 37 from the south fork). Since they are not significantly different, the solids export from the two forks can be weighted based on flow rate. Using mass balance calculations from conservative ions above and below the convergence of the two forks, the north fork was found to contribute an annually averaged 66% $\pm$ 12% of the total flow and south fork was found to contribute 34% $\pm$ 12% of the total flow. Accordingly, 66% of the TSS export was likely coming from agricultural lands (Table 5). Using the drainage areas and a measured bulk density of 0.8 g/cm^3 for the top 5 cm of soil, the TSS

export was converted to an areal solids loss from the two land uses. Unsurprisingly, the agriculture soil losses are larger than losses from the restored prairie. Although this estimate only accounts for sheet and rill erosion, this soil loss estimate is at the very low end of agricultural soil loss estimates, and is similar to soil formation rates (Montgomery 2007). The agricultural fields are terraced, minimally tilled, and there is a buffer of non-agricultural plants immediately surrounding the stream. Consequently, the combination of these soil management practices appears to be limiting soil loss from agricultural land use in this watershed.

While there are some limitations to high-frequency automated sampling, one of the advantages is the ability to see processes at time scales that are not typically observable. One good example is the diel flow variability in the stream (Figure 5). While not confirmed, a likely explanation of this variability is the increased evapotranspiration during daylight hours (Gribovszki, Szilágyi, and Kalicz 2010). When plants are respiring, they draw down the local groundwater table, lowering stream flow rates. When respiration slows during the night, the withdrawals also slow, allowing for recharge of the groundwater and increases to stream flow. While the diel cycle is generally better documented in forested systems (Gribovszki, Szilágyi, and Kalicz 2010), in a predominantly agricultural system underlain by similar soils found at Glacier Creek, the diel stream flow pattern has also been observed, but appears weaker than forested cycles (Loperfido et al. 2010). High frequency hydrogeochemical sampling in a temperate agricultural watershed in France similarly documented daily oscillations during a summer drought period (Floury et al. 2017). Furthermore, groundwater level variation has been observed under land uses dominated by native or invasive grass species (Schilling 2007, Soylu et al. 2012, Satchithanantham, Wilson, and Glenn 2017), with generally smaller groundwater drawdown compared to forested systems. Since Glacier Creek is predominantly groundwater fed, it seems likely that the flow rate cycling in the stream is related to changing groundwater levels caused by the vegetation.

Another observation within the turbidity data is the possibility of animal contributions to the solids flux. At many times throughout the year, there is an approximately 2-hour period just before dawn (~4:00-6:00) during which the turbidities increase as much as an order of magnitude before returning to baseline. This pre-dawn signal is present for several days before disappearing, only to show up again weeks or months later. There is no hydrogeochemical reason for these small, but consistent, changes to turbidity, so biological contributors are suspected. While not confirmed, one of any number of animals known to be present at the site (most notably the North American Racoon, *P. lotor*) may be disturbing the stream sediments with their pre-dawn activities. This is not likely a significant contributor to the overall solids flux due to the small time periods, and relatively modest changes to turbidity, however it would not be observed without regular high frequency sampling.

5.0 Conclusions

Using high-frequency sampling devices allows for quantifying environmental processes that would not be detectable with manual sampling timeframes. With the deployment of two high-frequency sampling devices, we were able to quantitate the flow, conductivity, and turbidity at 15-minute intervals in a stream the drains both restored prairie and agricultural land uses. Using chemical analyses of the solids concentration, the measured chemical parameters were converted to TDS and TSS concentrations. Using the solids concentrations and the flow values allowed for the calculation of flux values for a twelve-month period. TDS dominated the solids export in this catchment, but the TSS came predominantly from the agricultural lands. Formal error propagation gave relative errors of 0.1% on the annual TDS flux and 4.0% on the TSS flux. However, due to the nature of the sampling system, up to 20.1% of the TDS flux and 36.8% of the TSS flux was based on filling in missing data from the automated system. This range of values for both TDS and TSS essentially give a best- and worst-case scenario for the error estimates on the flux values. From sub-sampling the data at timescales longer than 15 minutes, we were able to examine the changes in the flux estimates based on sampling hourly, daily, weekly and

monthly. There were no consistent changes in either the flux value or the associated error as the sampling time period got longer. However, sampling monthly for TDS gave a flux value that was only 11% smaller than the value obtained at 15-minute intervals, and sampling TSS only during precipitation events captured 67% of the annual flux. Examining the data from precipitation events, a clockwise hysteresis pattern was generally observed for both conductivity and turbidity. For closely spaced rain events, the amount of hysteresis decreased suggesting an exhaustion of the pool of material available for export. Furthermore, precipitation rates <1.5 mm/hour led to no observable hysteretic pattern, suggesting that the system is able to store and slowly release that amount of water. From the flux values, overall soil loss due to rill and sheet erosion was found to be very low for both the agricultural (0.060 mm/yr) and restored prairie (0.019 mm/year) land uses.

CRediT authorship contribution statement

Andrew Miller: Conceptualization, Validation, Formal analysis, Writing-Original Draft, Visualization; **Ashlee Dere**: Conceptualization, Formal analysis, Writing- Review and Editing, Visualization; **Tracy Coleman**: Investigation, Data Curation, Writing- Review and Editing.

Declaration of competing interest

The authors declare that they have no known competing financial interest or personal relationships that could have appeared to the influence the work reported in this paper.

Acknowledgements

The authors would like to thank Tom Bragg and Barbi Hayes for their support of research at Glacier Creek Preserve, and Douglas County Nebraska Natural Resources District for instrumentation support. We also thank Mara Bullock, Dominick Caniglia, and Amy Hemje for additional field sampling assistance.

Appendix A. Supplementary data

Supplementary data regarding calibration records and precipitation events can be found in Appendix A.

References

Aubert, A. H., C. Gascuel-Odoux, G. Gruau, N. Akkal, M. Faucheux, Y. Fauvel, C. Grimaldi, Y. Hamon, A. Jaffrézic, M. Lecoz-Boutnik, J. Molénat, P. Petitjean, L. Ruiz, and P. Merot. 2013. "Solute transport dynamics in small, shallow groundwater-dominated agricultural catchments: insights from a high-frequency, multisolute 10 yr-long monitoring study." *Hydrol. Earth Syst. Sci.* 17 (4):1379-1391. doi: 10.5194/hess-17-1379-2013.

Birgand, F., C. Faucheux, G. Gruau, B. Augeard, F. Moatar, and P. Bordenave. 2010. "Uncertainties in Assessing Annual Nitrate Loads and Concentration Indicators: Part 1. Impact of Sampling

Frequency and Load Estimation Algorithms." *Transactions of the ASABE* 53 (2):437-446. doi: https://doi.org/10.13031/2013.29584.

Bragg, Tom, Craig Maier, and Yari Johnson. 2016. "09. Matching Long-Term Fire Effects Research to Pressing Questions Facing Tallgrass Prairie Managers Across the Upper Midwest." North American Prairie Conference Proceedings.

Burns, Douglas A., Brian A. Pellerin, Matthew P. Miller, Paul D. Capel, Anthony J. Tesoriero, and Jonathan M. Duncan. 2019. "Monitoring the riverine pulse: Applying high-frequency nitrate data to advance integrative understanding of biogeochemical and hydrological processes." *Wiley Interdisciplinary Reviews: Water* 6 (4):e1348. doi: 10.1002/wat2.1348.

Dere, Ashlee L., Andrew W. Miller, Amy M. Hemje, Sara K. Parcher, Courtney A. Capalli, and E. Arthur Bettis. 2019. "Solute Fluxes Through Restored Prairie and Intensively Managed Critical Zones in Nebraska and Iowa." *Frontiers in Earth Science* 7 (24). doi: 10.3389/feart.2019.00024.

Dickson, Timothy L., Barbara A. Hayes, and Thomas B. Bragg. 2019. "Effects of 34 Years of Experimentally Manipulated Burn Seasons and Frequencies on Prairie Plant Composition." *Rangeland Ecology & Management* 72 (1):82-91. doi: https://doi.org/10.1016/j.rama.2018.07.014.

Dupas, Rémi, Seifeddine Jomaa, Andreas Musolff, Dietrich Borchardt, and Michael Rode. 2016. "Disentangling the influence of hydroclimatic patterns and agricultural management on river nitrate dynamics from sub-hourly to decadal time scales." *Science of The Total Environment* 571:791-800. doi: https://doi.org/10.1016/j.scitotenv.2016.07.053.

Floury, P., J. Gaillardet, E. Gayer, J. Bouchez, G. Tallec, P. Ansart, F. Koch, C. Gorge, A. Blanchouin, and J. L. Roubaty. 2017. "The potamochemical symphony: new progress in the high-frequency acquisition of stream chemical data." *Hydrol. Earth Syst. Sci.* 21 (12):6153-6165. doi: 10.5194/hess-21-6153-2017.

Floury, Paul, Jérôme Gaillardet, Gaëlle Tallec, Patrick Ansart, Julien Bouchez, Pascale Louvat, and Caroline Gorge. 2019. "Chemical weathering and CO2 consumption rate in a multilayered-aquifer dominated watershed under intensive farming: The Orgeval Critical Zone Observatory, France." *Hydrological Processes* 33 (2):195-213. doi: 10.1002/hyp.13340.

Flávio, H. M., P. Ferreira, N. Formigo, and J. C. Svendsen. 2017. "Reconciling agriculture and stream restoration in Europe: A review relating to the EU Water Framework Directive." *Science of The Total Environment* 596-597:378-395. doi: https://doi.org/10.1016/j.scitotenv.2017.04.057.

Grathwohl, Peter, Hermann Rügner, Thomas Wöhling, Karsten Osenbrück, Marc Schwientek, Sebastian Gayler, Ute Wollschläger, Benny Selle, Marion Pause, Jens-Olaf Delfs, Matthias Grzeschik, Ulrich Weller, Martin Ivanov, Olaf A. Cirpka, Ulrich Maier, Bertram Kuch, Wolfgang Nowak, Volker Wulfmeyer, Kirsten Warrach-Sagi, Thilo Streck, Sabine Attinger, Lars Bilke, Peter Dietrich, Jan H. Fleckenstein, Thomas Kalbacher, Olaf Kolditz, Karsten Rink, Luis Samaniego, Hans-Jörg Vogel, Ulrike Werban, and Georg Teutsch. 2013. "Catchments as reactors: a comprehensive approach for water fluxes and solute turnover." *Environmental Earth Sciences* 69 (2):317-333. doi: 10.1007/s12665-013-2281-7.

Gribovszki, Zoltán, József Szilágyi, and Péter Kalicz. 2010. "Diurnal fluctuations in shallow groundwater levels and streamflow rates and their interpretation – A review." *Journal of Hydrology* 385 (1):371-383. doi: https://doi.org/10.1016/j.jhydrol.2010.02.001.

Harmel, R. D., D. R. Smith, K. W. King, and R. M. Slade. 2009. "Estimating storm discharge and water quality data uncertainty: A software tool for monitoring and modeling applications." *Environmental Modelling & Software* 24 (7):832-842. doi: https://doi.org/10.1016/j.envsoft.2008.12.006.

Hem, J.D. 1982. "Chapter 4-Conductance: A collective measure of dissolved ions." In *Water Analysis Volume I Inorganic Species*, edited by R.A. Miner and L.H. Keith. New York, New York: Academic Press.

Horsburgh, Jeffery S., Amber Spackman Jones, David K. Stevens, David G. Tarboton, and Nancy O. Mesner. 2010. "A sensor network for high frequency estimation of water quality constituent fluxes using surrogates." *Environmental Modelling & Software* 25 (9):1031-1044. doi: https://doi.org/10.1016/j.envsoft.2009.10.012.

Jeong, Jong-Jin, Svenja Bartsch, Jan H. Fleckenstein, Egbert Matzner, John D. Tenhunen, Sang Don Lee, Seon Ki Park, and Ji-Hyung Park. 2012. "Differential storm responses of dissolved and particulate organic carbon in a mountainous headwater stream, investigated by high-frequency, in situ optical measurements." *Journal of Geophysical Research: Biogeosciences* 117 (G3). doi: 10.1029/2012jg001999.

Jones, Amber Spackman, Jeffery S. Horsburgh, Nancy O. Mesner, Ronald J. Ryel, and David K. Stevens. 2012. "Influence of Sampling Frequency on Estimation of Annual Total Phosphorus and Total Suspended Solids Loads1." *JAWRA Journal of the American Water Resources Association* 48 (6):1258-1275. doi: 10.1111/j.1752-1688.2012.00684.x.

Jones, Amber Spackman, David K. Stevens, Jeffery S. Horsburgh, and Nancy O. Mesner. 2011. "Surrogate Measures for Providing High Frequency Estimates of Total Suspended Solids and Total Phosphorus Concentrations1." *JAWRA Journal of the American Water Resources Association* 47 (2):239-253. doi: 10.1111/j.1752-1688.2010.00505.x.

Kerr, Jason G., M. Catherine Eimers, and Huaxia Yao. 2016. "Estimating stream solute loads from fixed frequency sampling regimes: the importance of considering multiple solutes and seasonal fluxes in the design of long-term stream monitoring networks." *Hydrological Processes* 30 (10):1521-1535. doi: 10.1002/hyp.10733.

Kerr, Jason G., James P. Zettel, Cynthia N. McClain, and Mary K. Kruk. 2018. "Monitoring heavy metal concentrations in turbid rivers: Can fixed frequency sampling regimes accurately determine criteria exceedance frequencies, distribution statistics and temporal trends?" *Ecological Indicators* 93:447-457. doi: https://doi.org/10.1016/j.ecolind.2018.05.028.

Khamis, K., C. Bradley, and D. M. Hannah. 2020. "High frequency fluorescence monitoring reveals new insights into organic matter dynamics of an urban river, Birmingham, UK." *Science of The Total Environment* 710:135668. doi: https://doi.org/10.1016/j.scitotenv.2019.135668.

Li, Ying, Haw Yen, R. Daren Harmel, Qiuliang Lei, Jiaogen Zhou, Wanli Hu, Wenchao Li, Huishu Lian, A. Xing Zhu, Limei Zhai, Hongyuan Wang, Weiwen Qiu, Jiafa Luo, Shuxia Wu, Hongbin Liu, and Xiaohong Li. 2019. "Effects of sampling strategies and estimation algorithms on total nitrogen load determination in a small agricultural headwater watershed." *Journal of Hydrology* 579:124114. doi: https://doi.org/10.1016/j.jhydrol.2019.124114.

Lin, Guan-Wei, Hongey Chen, Dave N. Petley, Ming-Jame Horng, Shuei-Ji Wu, and Bin Chuang. 2011. "Impact of rainstorm-triggered landslides on high turbidity in a mountain reservoir." *Engineering Geology* 117 (1):97-103. doi: https://doi.org/10.1016/j.enggeo.2010.10.009.

Line, D.E., K.R. Hall, and J.D. Blackwell. 2013. "Estimating Suspended Solids from Turbidity in the Robeson Creek, NC Watershed." *JAWRA Journal of the American Water Resources Association* 49 (6):1412-1420. doi: 10.1111/jawr.12094.

Liu, Wenlong, Mohamed A. Youssef, François P. Birgand, George M. Chescheir, Shiying Tian, and Bryan M. Maxwell. 2020. "Processes and mechanisms controlling nitrate dynamics in an artificially drained field: Insights from high-frequency water quality measurements." *Agricultural Water Management* 232:106032. doi: https://doi.org/10.1016/j.agwat.2020.106032.

Lloyd, C. E. M., J. E. Freer, P. J. Johnes, and A. L. Collins. 2016. "Using hysteresis analysis of high-resolution water quality monitoring data, including uncertainty, to infer controls on nutrient and sediment transfer in catchments." *Science of The Total Environment* 543:388-404. doi: https://doi.org/10.1016/j.scitotenv.2015.11.028.

Loperfido, J. V., Craig L. Just, Athanasios N. Papanicolaou, and Jerald L. Schnoor. 2010. "In situ sensing to understand diel turbidity cycles, suspended solids, and nutrient transport in Clear Creek, Iowa." *Water Resources Research* 46 (6). doi: 10.1029/2009wr008293.

Miller, Matthew P., Anthony J. Tesoriero, Paul D. Capel, Brian A. Pellerin, Kenneth E. Hyer, and Douglas A. Burns. 2016. "Quantifying watershed-scale groundwater loading and in-stream fate of nitrate using high-frequency water quality data." *Water Resources Research* 52 (1):330-347. doi: 10.1002/2015wr017753.

Miller, Matthew P., Anthony J. Tesoriero, Krista Hood, Silvia Terziotti, and David M. Wolock. 2017. "Estimating Discharge and Nonpoint Source Nitrate Loading to Streams From Three End-Member Pathways Using High-Frequency Water Quality Data." *Water Resources Research* 53 (12):10201-10216. doi: 10.1002/2017wr021654.

Montgomery, David R. 2007. "Soil erosion and agricultural sustainability." *Proceedings of the National Academy of Sciences* 104 (33):13268-13272. doi: 10.1073/pnas.0611508104.

Nasrabadi, T., H. Ruegner, Z. Z. Sirdari, M. Schwientek, and P. Grathwohl. 2016. "Using total suspended solids (TSS) and turbidity as proxies for evaluation of metal transport in river water." *Applied Geochemistry* 68:1-9. doi: https://doi.org/10.1016/j.apgeochem.2016.03.003.

Neal, Colin, Brian Reynolds, Philip Rowland, David Norris, James W. Kirchner, Margaret Neal, Darren Sleep, Alan Lawlor, Clive Woods, Sarah Thacker, Hayley Guyatt, Colin Vincent, Kathryn Hockenhull, Heather Wickham, Sarah Harman, and Linda Armstrong. 2012. "High-frequency water quality time series in precipitation and streamflow: From fragmentary signals to scientific challenge." *Science of The Total Environment* 434:3-12. doi: https://doi.org/10.1016/j.scitotenv.2011.10.072.

Nimick, David A., Christopher H. Gammons, and Stephen R. Parker. 2011. "Diel biogeochemical processes and their effect on the aqueous chemistry of streams: A review." *Chemical Geology* 283 (1):3-17. doi: https://doi.org/10.1016/j.chemgeo.2010.08.017.

Parkhurst, D.L., and C. A. J. Appelo. 2013. "Description of input and examples for PHREEQC version 3 — A computer program for speciation, batc h-reaction, one-dimensional transport, and inverse geochemical calculations." In *Techniques and Methods*, 497. Denver, CO: U.S. Geological Survey Water Resources.

Pellerin, Brian A., Brian A. Bergamaschi, Robert J. Gilliom, Charles G. Crawford, JohnFranco Saraceno, C. Paul Frederick, Bryan D. Downing, and Jennifer C. Murphy. 2014. "Mississippi River Nitrate Loads from High Frequency Sensor Measurements and Regression-Based Load Estimation." *Environmental Science & Technology* 48 (21):12612-12619. doi: 10.1021/es504029c.

Rode, Michael, Andrew J. Wade, Matthew J. Cohen, Robert T. Hensley, Michael J. Bowes, James W. Kirchner, George B. Arhonditsis, Phil Jordan, Brian Kronvang, Sarah J. Halliday, Richard A. Skeffington, Joachim C. Rozemeijer, Alice H. Aubert, Karsten Rinke, and Seifeddine Jomaa. 2016. "Sensors in the Stream: The High-Frequency Wave of the Present." *Environmental Science & Technology* 50 (19):10297-10307. doi: 10.1021/acs.est.6b02155.

Rügner, Hermann, Marc Schwientek, Barbara Beckingham, Bertram Kuch, and Peter Grathwohl. 2013. "Turbidity as a proxy for total suspended solids (TSS) and particle facilitated pollutant transport in catchments." *Environmental Earth Sciences* 69 (2):373-380. doi: 10.1007/s12665-013-2307-1.

Satchithanantham, Sanjayan, Henry F. Wilson, and Aaron J. Glenn. 2017. "Contrasting patterns of groundwater evapotranspiration in grass and tree dominated riparian zones of a temperate agricultural catchment." *Journal of Hydrology* 549:654-666. doi: https://doi.org/10.1016/j.jhydrol.2017.04.016.

Schilling, Keith E. 2007. "Water table fluctuations under three riparian land covers, Iowa (USA)." *Hydrological Processes* 21 (18):2415-2424. doi: 10.1002/hyp.6393.

Schleppi, Patrick, Peter A. Waldner, and Bruno Fritschi. 2006. "Accuracy and precision of different sampling strategies and flux integration methods for runoff water: comparisons based on measurements of the electrical conductivity." *Hydrological Processes* 20 (2):395-410. doi: 10.1002/hyp.6057.

Schwarz, Kerstin, Tilman Gocht, and Peter Grathwohl. 2011. "Transport of polycyclic aromatic hydrocarbons in highly vulnerable karst systems." *Environmental Pollution* 159 (1):133-139. doi: https://doi.org/10.1016/j.envpol.2010.09.026.

Schwientek, Marc, Karsten Osenbrück, and Matthias Fleischer. 2013. "Investigating hydrological drivers of nitrate export dynamics in two agricultural catchments in Germany using high-frequency data series." *Environmental Earth Sciences* 69 (2):381-393. doi: 10.1007/s12665-013-2322-2.

Snyder, Lisle, Jody D. Potter, and William H. McDowell. 2018. "An Evaluation of Nitrate, fDOM, and Turbidity Sensors in New Hampshire Streams." *Water Resources Research* 54 (3):2466-2479. doi: 10.1002/2017wr020678.

Soylu, Mehmet Evren, John D. Lenters, Erkan Istanbulluoglu, and Steven P. Loheide II. 2012. "On evapotranspiration and shallow groundwater fluctuations: A Fourier-based improvement to the White method." *Water Resources Research* 48 (6). doi: 10.1029/2011wr010964.

Stubblefield, Andrew P., John E. Reuter, Randy A. Dahlgren, and Charles R. Goldman. 2007. "Use of turbidometry to characterize suspended sediment and phosphorus fluxes in the Lake Tahoe basin, California, USA." *Hydrological Processes* 21 (3):281-291. doi: 10.1002/hyp.6234.

Thompson, Joshua, Rachel Cassidy, Donnacha G. Doody, and Ray Flynn. 2014. "Assessing suspended sediment dynamics in relation to ecological thresholds and sampling strategies in two Irish headwater catchments." *Science of The Total Environment* 468-469:345-357. doi: https://doi.org/10.1016/j.scitotenv.2013.08.069.

USDA. 2016. The Convervation reserve Program: 49th Signup Results. edited by Farm Service Agency U.S. Department of Agriculture. Washington D.C.

von Freyberg, J., B. Studer, and J. W. Kirchner. 2017. "A lab in the field: high-frequency analysis of water quality and stable isotopes in stream water and precipitation." *Hydrol. Earth Syst. Sci.* 21 (3):1721-1739. doi: 10.5194/hess-21-1721-2017.

Wymore, Adam S., Miguel C. Leon, James B. Shanley, and William H. McDowell. 2019. "Hysteretic Response of Solutes and Turbidity at the Event Scale Across Forested Tropical Montane Watersheds." *Frontiers in Earth Science* 7 (126). doi: 10.3389/feart.2019.00126.

Ziegler, Alan D., Shawn G. Benner, Chatchai Tantasirin, Spencer H. Wood, Ross A. Sutherland, Roy C. Sidle, Nicholas Jachowski, Mike A. Nullet, Lu Xi Xi, Anond Snidvongs, Thomas W. Giambelluca, and Jefferson M. Fox. 2014. "Turbidity-based sediment monitoring in northern Thailand: Hysteresis, variability, and uncertainty." *Journal of Hydrology* 519:2020-2039. doi: https://doi.org/10.1016/j.jhydrol.2014.09.010.

Zimmer, Margaret A., Brian Pellerin, Douglas A. Burns, and Gregory Petrochenkov. 2019. "Temporal Variability in Nitrate-Discharge Relationships in Large Rivers as Revealed by High-Frequency Data." *Water Resources Research* 55 (2):973-989. doi: 10.1029/2018wr023478.

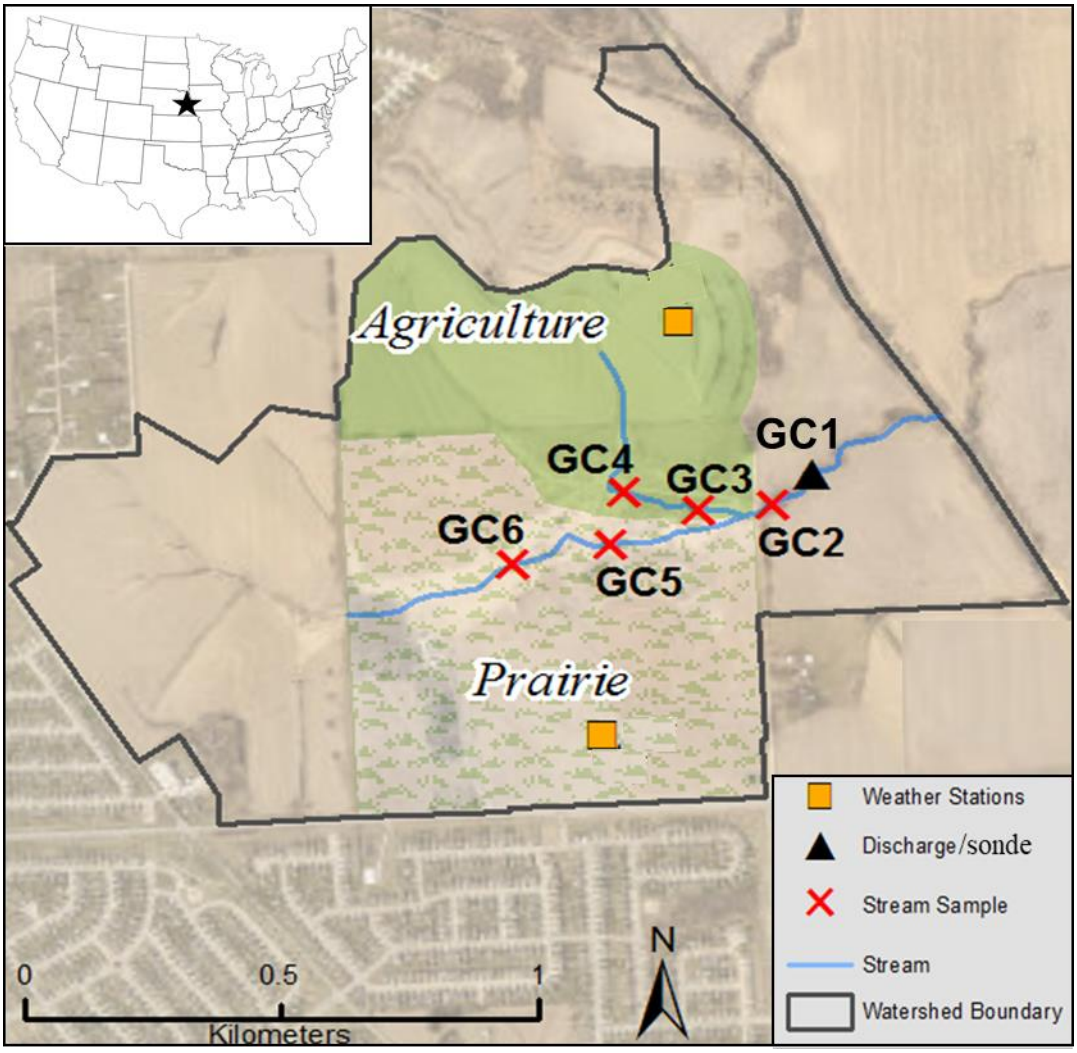

Figure 1 Glacier Creek Preserve, a 2.1 km^2 first order watershed located in Eastern Nebraska, USA. A multiparameter sonde and discharge sensor (black triangle) are installed at the outlet of Glacier Creek, and monthly stream samples were collected just downstream of the sonde (GC1), at two locations on a tributary draining agricultural land use (GC3, GC4), at two locations draining restored prairie land use (GC5, GC6), and at the confluence of the two tributaries (GC2). Weather stations in each land use measure basic meteorological data.

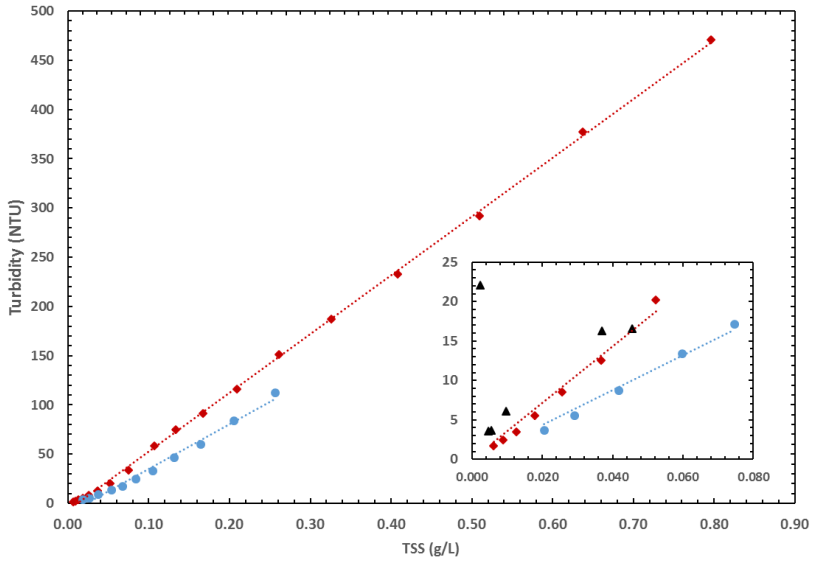

Figure 2- Turbidity relationship to TSS. The blue circles represent the solids from the 25-Jun-2019 collection event described in the text, the red diamonds are from the 16-Jul-2019 event. The black triangles in the inset are from the grab samples that were analyzed independently of the solids collection.

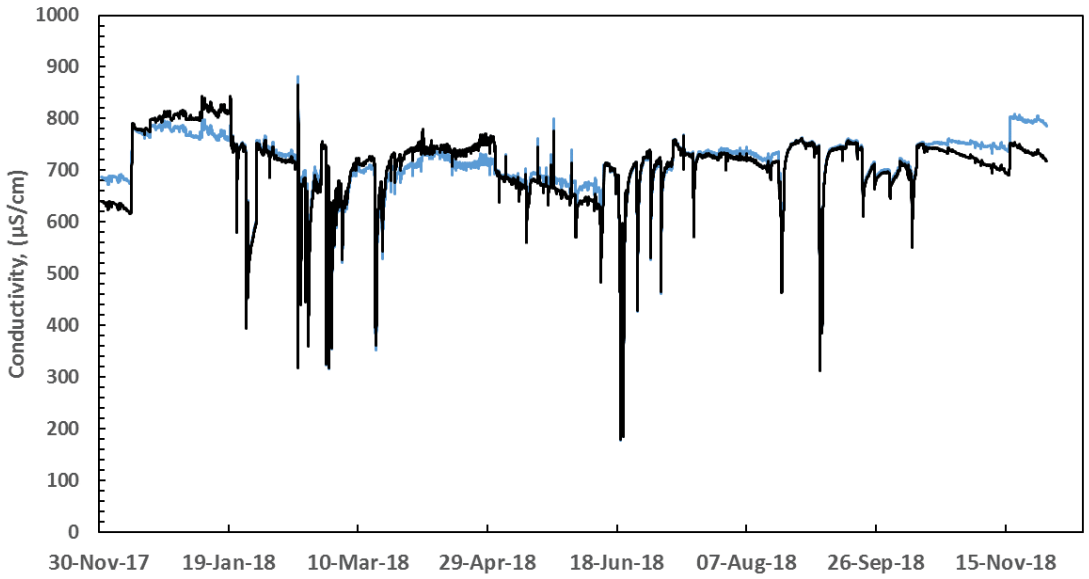

826

827 **Figure 3-** Conductivity values as a function of time. The blue line is the uncorrected values, the black line
828 has been corrected for changes in calibration.

829

830

831

832

833

834

835

836

837

838

839

840

841

842

843

844

845

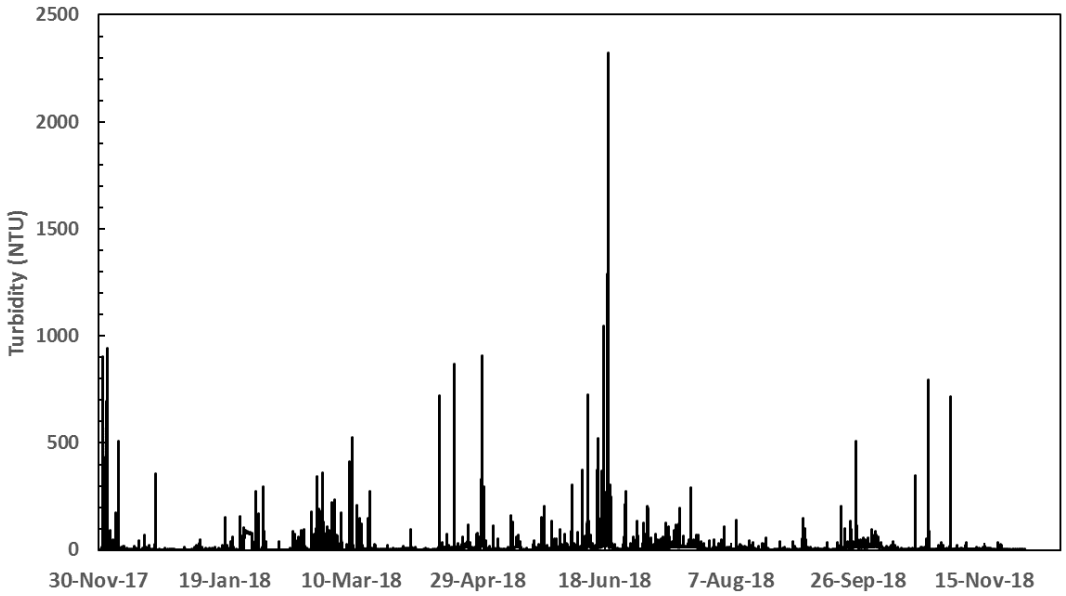

Figure 4- Turbidity values as a function of time.

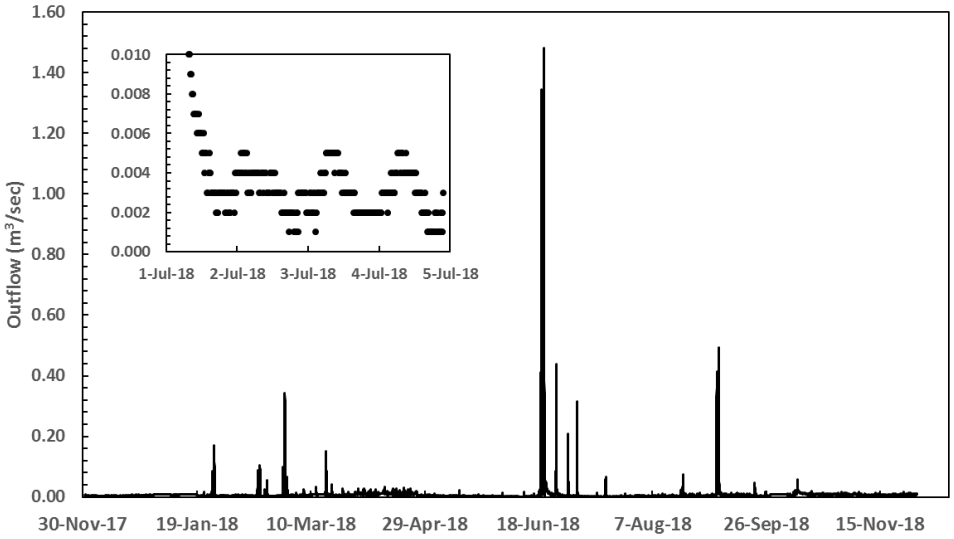

Figure 5- Outflow volume as a function of time. The inset shows a 5-day period in mid-summer immediately following a rain event.

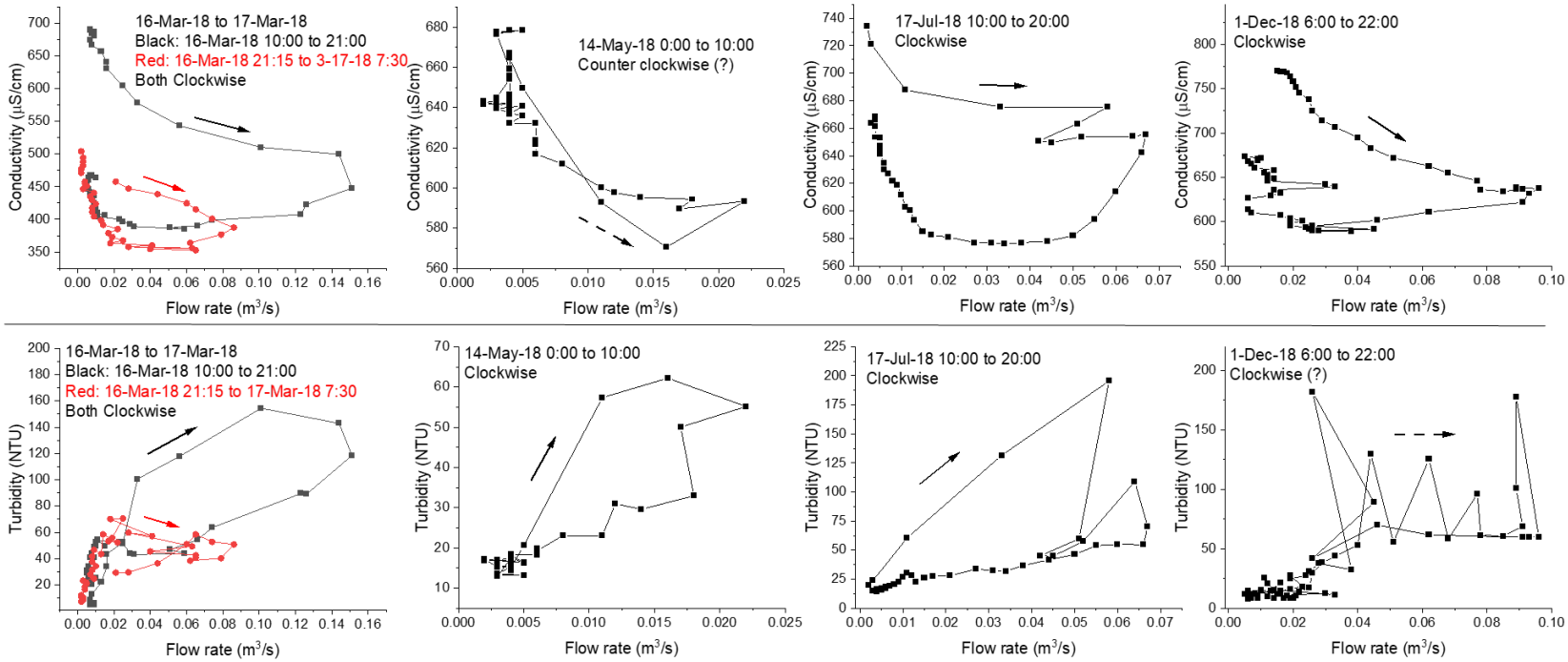

884

885 **Figure 6-** Examples of conductivity (top row) and turbidity (bottom row) hysteresis loops exhibiting generally clockwise hysteresis during four
886 precipitation different events throughout the year. Note variable scale across plots.

887

888

889

890

891

892

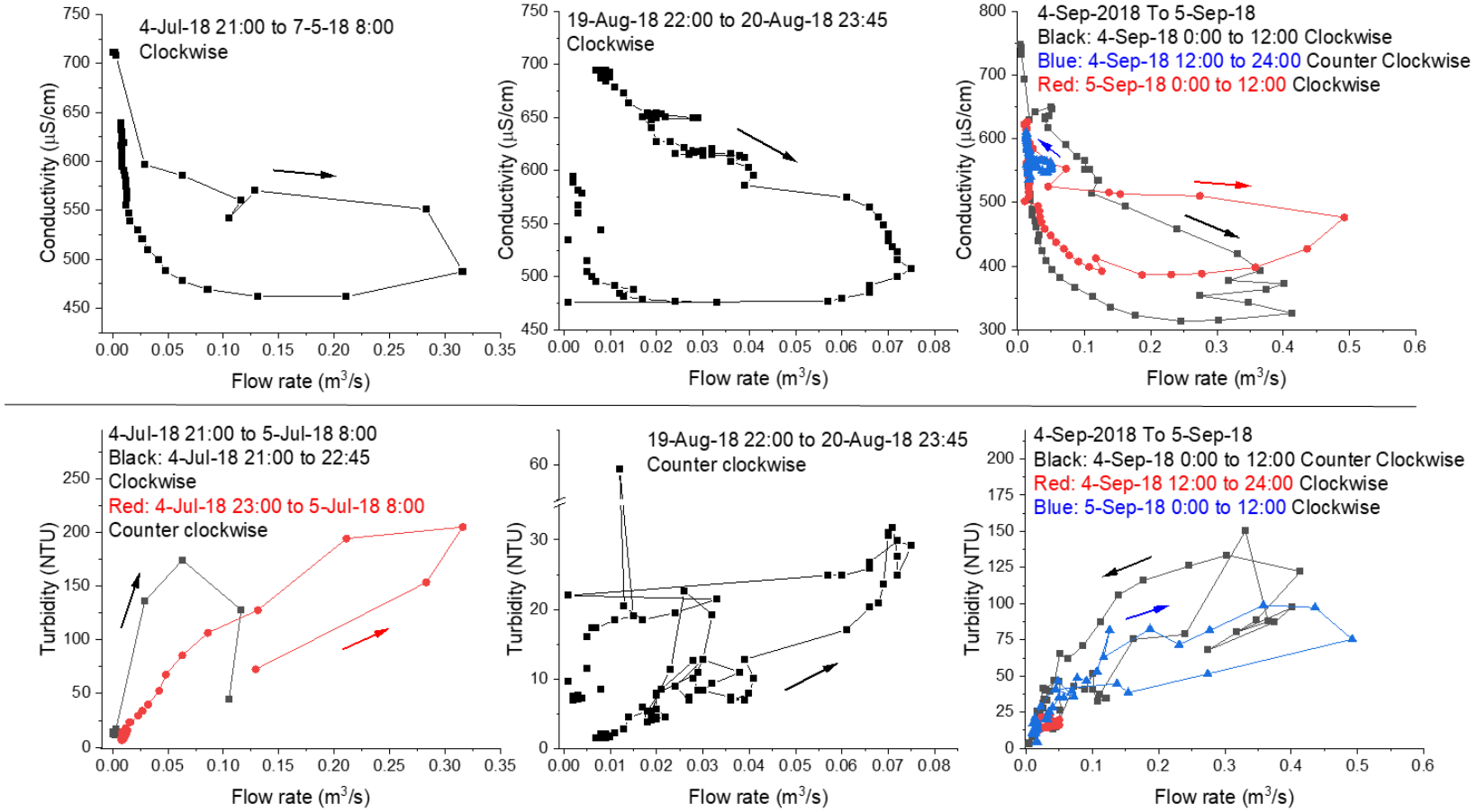

Figure 7- Examples of conductivity (top row) and turbidity (bottom row) hysteresis loops exhibiting clockwise hysteresis behavior for conductivity but complex hysteresis behavior for turbidity during three different precipitation events. Note variable scales across plots.

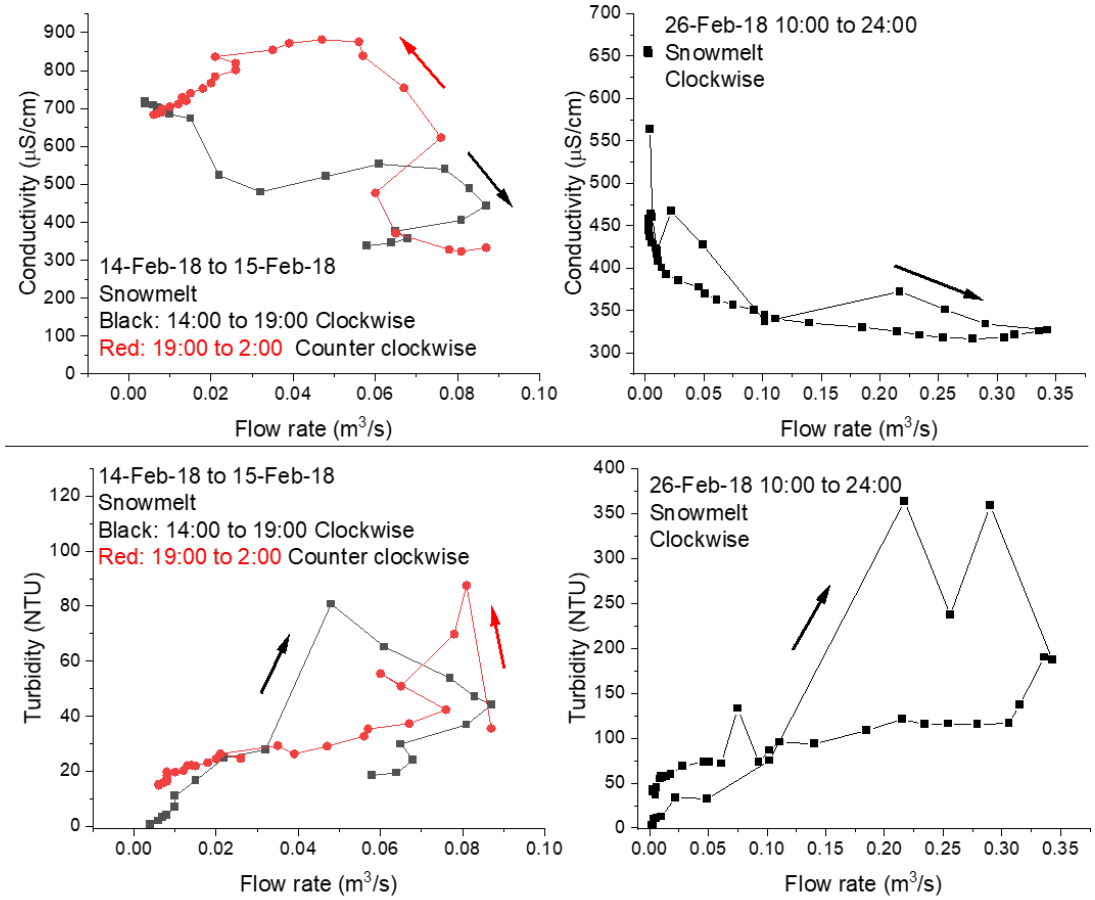

Figure 8- Examples of conductivity (top row) and turbidity (bottom row) hysteresis loops during two different snowmelt events. Note variable scale across plots.

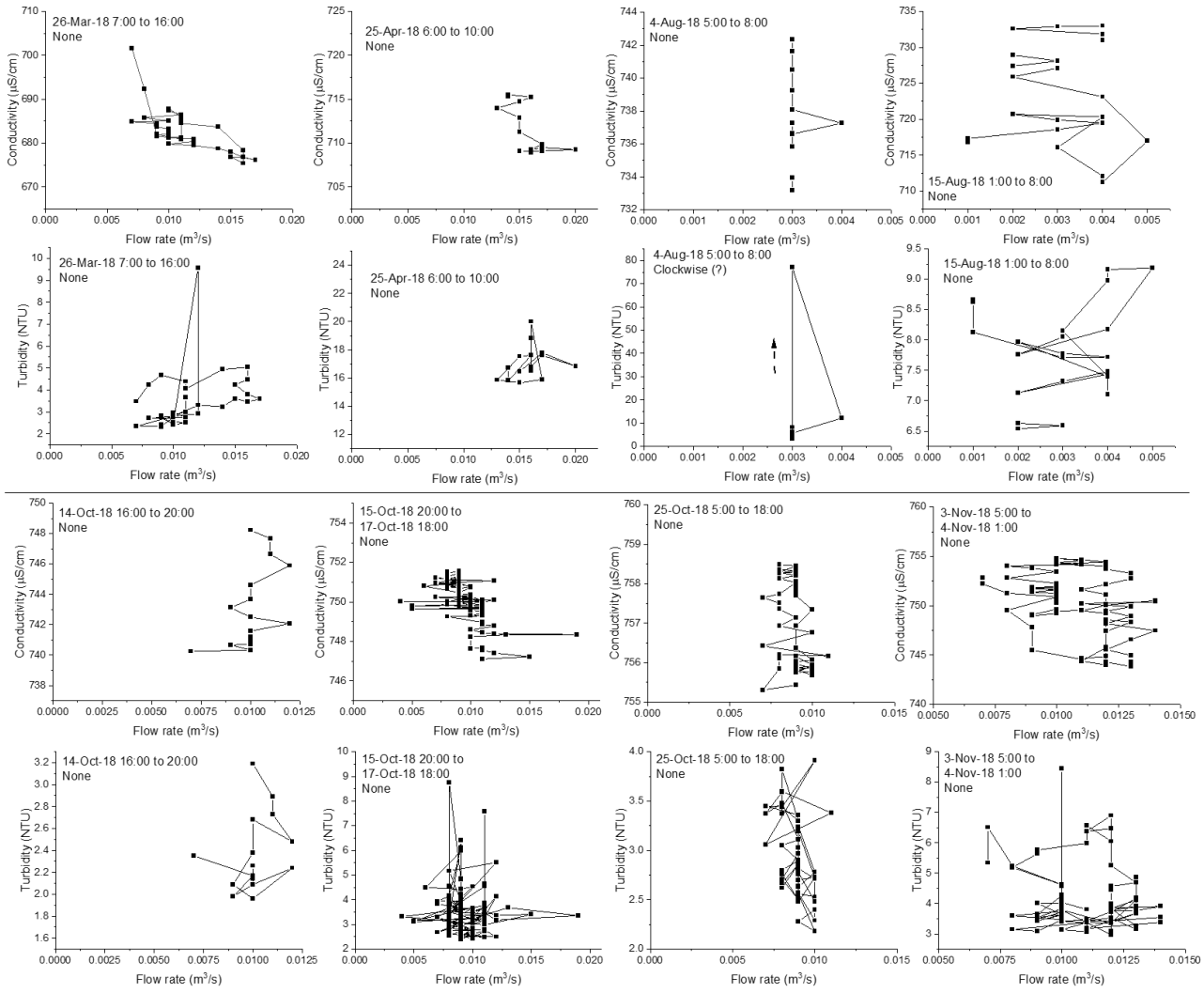

Figure 9- Examples of conductivity (top and third from top row) and turbidity (second from top and bottom row) precipitation events exhibiting no hysteresis behavior (lack of directionality) during eight different precipitation events throughout the year. Rainfall intensity during these events was <1.5 mm/hr. Note variable scale across plots and generally small changes in conductivity or turbidity and flow.

Table 1- Average, standard deviation, and number of measurements for conductivity and turbidity. GC3/GC4 is in the north fork drainage, which is mostly agricultural. Positions GC5/GC6 represent the south fork, which mostly drains restored prairie.

Positions-Parameter	Average	Std. Dev.	n
GC3/GC4- conductivity	680 µS/cm	45	44
GC5/GC6- conductivity	907 µS/cm	72	44
GC3/GC4- turbidity	9.7 NTU	15	29
GC5/GC6- turbidity	11.7NTU	15	37

Table 2- Equations and correlation coefficients for the lines of best fit shown in Figure 1. The equations that were actually used are also shown.

Condition	Equation for the line	R^2	Equation used
<20 NTU, 25-Jun-2019	Turb. = 219.94(TSS)	0.9813	Turb. = 288.48(TSS); R^2 = 0.7422
<20 NTU, 16-Jul-2019	Turb. = 357.48(TSS)	0.9792	
>20 NTU, 25-Jun-2019	Turb. = 596.39(TSS) - 6.7259	0.9995	Turb. = 596.39(TSS) - 6.7259; R^2 =
>20 NTU, 16-Jul-2019	Turb. = 408.04(TSS) - 10.345	0.9872	0.9995

Table 3- Annual flux estimates and associated errors for TDS and TSS. All values are kg/year. All error estimates were rounded to three digits.

	Sampling interval				
	15 minutes	Hourly	Daily	Weekly	Monthly
TDS	75,259	75,259	76,440	76,012	67,335
TDS (std. dev.)	88	288	5230	22,800	15,600
TDS (90% CI)		339	2710	8590	3950
TSS	23,099	23,099	41,068	45,180	4680
TSS (std. dev.)	921	4397	75,400	127,000	4280
TSS (90% CI)		5174	38,600	47,900	1080
n	1	4	12	21	44

Table 4- The proportion of time where extrapolated data was used, and the proportion of the flux associated with extrapolated data. For the missing flow data, values in parentheses are for data gaps <1 hour in duration.

Condition	% of data points	% of total TDS flux	% of total TSS flux
Missing flow data	24.7 (18.0)	20.1 (16.5)	36.8 (30.9)
Missing turbidity and/or flow data	3.9		36.9
Missing conductivity and/or flow data	0.7	20.6	
Turbidity >124 NTU	0.7		67.0

Table 5- Drainage area and separation of the total suspended solids flux from the two land uses. Values in parentheses are one standard deviation.

	Drainage area, km^2	Annualized % of total flow	Soil loss (g $soil*year^{-1}*m^{-2}$)	Soil depth loss ($mm*year^{-1}$)
North fork (agriculture)	0.536	66% (12%)	48.2 (9.3)	0.060
South fork (restored prairie)	0.315	34% (12%)	14.7 (5.4)	0.019